MAGNETISM

Singular angular magnetoresistance in a magnetic nodal semimetal

T. Suzuki[1], L. Savary[1,2,3], J.-P. Liu[2,4], J. W. Lynn[5], L. Balents[2], J. G. Checkelsky[1]*

Transport coefficients of correlated electron systems are often useful for mapping hidden phases with distinct symmetries. Here we report a transport signature of spontaneous symmetry breaking in the magnetic Weyl semimetal cerium-aluminum-germanium (CeAlGe) system in the form of singular angular magnetoresistance (SAMR). This angular response exceeding 1000% per radian is confined along the high-symmetry axes with a full width at half maximum reaching less than 1° and is tunable via isoelectronic partial substitution of silicon for germanium. The SAMR phenomena is explained theoretically as a consequence of controllable high-resistance domain walls, arising from the breaking of magnetic point group symmetry strongly coupled to a nearly nodal electronic structure. This study indicates ingredients for engineering magnetic materials with high angular sensitivity by lattice and site symmetries.

The past decade has revealed an unexpected depth of phenomena in topological aspects of electronic solids and in strongly spin-orbit–coupled materials (*1*–*9*). A key recent advance is the discovery of Weyl and Dirac fermions, which occur at topologically nontrivial points, known as "nodes," at which bulk bands cross (*10*–*14*). The band crossings themselves, and the surface Fermi arcs they engender, have been observed through angle-resolved photoemission (*15*, *16*). Transport studies detect pronounced longitudinal negative magnetoresistance, which may be attributed to the chiral anomaly of Weyl fermions (*17*, *18*).

It is known that Weyl fermions require breaking of either inversion or time-reversal symmetry. The former option is realized structurally in TaAs (*19*) and related materials. Magnetic Weyl semimetals, which evince the second possibility, have been harder to identify but have recently been discussed in systems such as $HgCr_2Se_4$ (*20*), *R*AlGe (where *R* is a rare-earth element) (*21*), $SrMnSb_2$ (*22*), and Mn_3Z (where *Z* is Ga, Sn, or Ge) (*23*, *24*). Magnetic Weyl semimetals could host controllable topological defects in the form of domain walls (DWs) that can be moved, created, and annihilated in situ in a single sample. It is intriguing to contemplate the interactions between these real-space topological defects and the Weyl points, which are momentum-space topological defects (*11*). More generally, substantial coupling of magnetic configurations to semimetallic electronic structure may afford technologically useful behavior for sensors and spintronic devices (*25*).

Here we identify a sharp signature of this interaction, singular angular magnetoresistance (SAMR) in $CeAlGe_{1-x}Si_x$ (crystal structure shown in Fig. 1A). SAMR is a pronounced enhancement of resistance occurring over a narrow angular range [down to full width at half maximum (FWHM) < 1°] leading to a derivative of resistance with respect to angle exceeding 1000% per radian, under particular conditions of applied magnetic fields (Fig. 1B). This is in clear contrast to conventional angular magnetoresistance (AMR), which describes a smooth dependence of resistivity ρ on the orientation of magnetization **M** and electrical current **I** in magnetic conductors (*26*). As depicted in Fig. 1C, we argue that this arises from momentum-space mismatch across real-space magnetic domains.

CeAlGe (x = 0) crystallizes in a nonsymmorphic tetragonal structure with space group $I4_1md$ (Fig. 1A) (*27*, *28*). The magnetic Ce ions (located at the Wyckoff 4*a* positions) comprise two interpenetrating body-centered–tetragonal sublattices (A and B) offset by 0, $a/2$, and $c/4$ along the [100], [010], and [001] direction, respectively. The lattice is tetragonal, but the Ce site has a lower orthorhombic symmetry 2*mm*. This orthorhombicity makes the local in-plane axes of each Ce ion inequivalent, resulting in an anisotropic g-tensor $g_{xx} \pm g_{yy}$ (with x and y parallel to the <100> tetragonal axes). Furthermore, the structure contains 4_1 (and 4_3) screw axis operations involving 90° rotations of the in-plane axes that interchange the Ce sublattices (*29*), thus making the g-tensor components g_{100} along the global [100] direction sublattice-dependent [$g_{100} = g_{xx}(g_{yy})$ for A (B)]. Consequently, the ordering of spins S^i (defined to have unit magnitude) and magnetic moments $m^i \equiv \frac{1}{2} g_{ij} \mu_B S^j$ can be qualitatively different (where μ_B is the Bohr magneton and $i, j = \{x, y, z\}$). As we describe below, this allows for an unusual ferrimagnetic magnetic moment **m** ordering in a conventional antiferromagnetic spin **S** network, with acute sensitivity to the magnetic point group. Although a range of magnetic ground states has been previously reported for CeAlGe attributed to the sensitivity of these materials to growth conditions (*27*, *30*–*32*), we find that this magnetic state is stabilized using chemical pressure with isoelectronic substitution of Ge by Si ($CeAlGe_{1-x}Si_x$) (*29*).

The most notable consequence of the above structure is the AMR observed in the longitudinal resistivity $\rho_{xx}(H, \theta)$ below the magnetic ordering temperature T_N = 5.6 K. This is shown for $CeAlGe_{0.72}Si_{0.28}$ at T = 2 K in Fig. 1B, where the current **I** is applied along [010] and $\mu_0 H$ = 2.2 T rotated in the tetragonal plane (θ is measured from [100] as shown in Fig. 1A; where μ_0 is the vacuum permeability and H is the magnetic field). A sharp enhancement is observed when θ is near the crystallographic high-symmetry directions <100>. This can be contrasted with the behavior at T = 6.5 K, which shows a smoothly varying profile captured by conventional AMR and has the symmetry of the underlying nonmagnetic group symmetry (*29*). This comparison is also shown in a polar plot in the inset of Fig. 1B where the sharpness of the features along all four tetragonal directions is apparent. Neutron scattering experiments show no sign of a structural transition at T_N (*29*), indicating instead that the SAMR is purely of magnetic origin.

A more detailed profile of $\rho_{xx}(\theta, H)$ is shown in Fig. 2A. With **H** aligned precisely along the [100] direction (θ = 0°), a prominent peak is observed in $\rho_{xx}(H)$, reaching a maximum near $\mu_0 H$ = 2 T. At higher H, this peak is suppressed and conventional magnetoresistance is seen. More notably, the peak signal rapidly disappears with increasing θ, whereas the remainder of $\rho_{xx}(H)$ remains unchanged: for θ = 0.7° the peak is largely suppressed and appears to completely vanish by θ = 1.5°. The field evolution of the magnetization $M(H)$ at the same T = 2 K is shown in Fig. 2B (θ = 0°). At a low field $\mu_0 H_0 \equiv 0.02$ T, a sharp rise in $M(H)$ is observed (inset) followed by a gentle increase toward a saturation moment of 0.97 μ_B/Ce. From the associated real part of the ac magnetic susceptibility χ' and its field derivative $d\chi'/dH$, two further field scales $\mu_0 H_1 \equiv 1.86$ T and $\mu_0 H_2 \equiv 3.28$ T can be identified, which bracket the $\rho_{xx}(H)$ peak associated with SAMR (marked by arrows in Fig. 2B). An alternate view of the SAMR regime with changing θ is shown in Fig. 2C, where outside of $H \in [H_1, H_2]$ a slowly varying θ dependence characteristic of conventional AMR is observed (*26*, *29*). Focusing on the SAMR region, the sharpest response is seen as a peak in $\rho_{xx}(\theta)$ for $\mu_0 H$ = 2.2 T with FWHM Δθ = 0.7°. The largest $\frac{d}{d\theta}\left(\frac{\rho_{xx}}{\rho_0}\right) \approx 1200\%$ radian^{-1} (ρ_0 is the zero-field resistivity) is two orders of magnitude larger than in permalloy (a conventional AMR material) (*26*), whereas the small Δθ is reminiscent of the response in $Sr_3Ru_2O_7$ (*33*, *34*) but is more than an order of magnitude narrower here.

[1]Department of Physics, Massachusetts Institute of Technology, Cambridge, MA 02139, USA. [2]Kavli Institute for Theoretical Physics, University of California, Santa Barbara, CA 93106, USA. [3]Université de Lyon, École Normale Supérieure de Lyon, Université Claude Bernard Lyon I, CNRS, Laboratoire de Physique, 46 Allée d'Italie, 69007 Lyon, France. [4]Department of Physics, The Hong Kong University of Science and Technology, Kowloon, Hong Kong. [5]NIST Center for Neutron Research, National Institute of Standards and Technology, Gaithersburg, MD 20899, USA.
*Corresponding author. Email: checkelsky@mit.edu

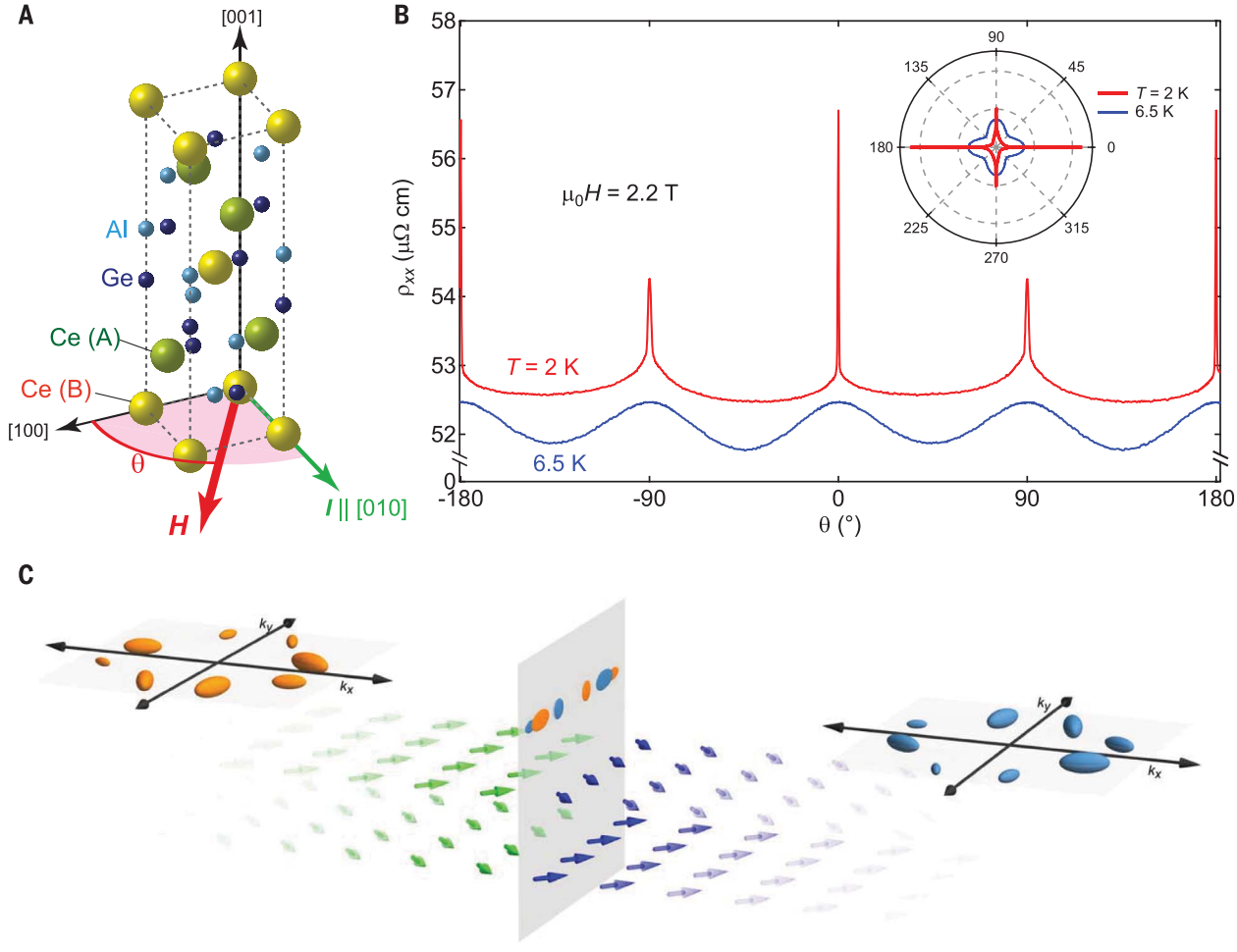

Fig. 1. Singular angular magnetoresistance (SAMR). (**A**) Crystal structure of CeAlGe (space group $I4_1md$). The measurement configuration for SAMR is shown with the field **H** rotation angle θ in the *ab* plane. (**B**) Angular θ dependence of the longitudinal resistivity ρ_{xx} of $CeAlGe_{0.72}Si_{0.28}$ in the magnetically ordered (T = 2 K) and paramagnetic (T = 6.5 K) phases. The curve for T = 6.5 K is offset by −9.5 microhm·cm for clarity. The inset displays the corresponding polar plot. The data at T = 2 K (T = 6.5 K) are offset by −52.2 microhm·cm (−60.5 microhm·cm). (**C**) Depiction in real and momentum space of the origin of SAMR in a magnetic nodal semimetal. A magnetic domain boundary is shown in real space as a vertical gray plane, which separates two distinct spin configurations drawn as green and blue arrows. The momentum-space Fermi surfaces are shown on either side as orange and blue ellipsoids and projected onto the plane of the DW. A minimal Fermi surface overlap leads to a large DW resistance; coupling of the nodal structure to the magnetic point group allows acute sensitivity of this effect to symmetry. Here the magnetic field is applied along the *x* direction corresponding to [100].

We now argue that the observed angular magnetoresistance phenomena signify magnetic quantum phase transitions and broken magnetic point group symmetry in the intermediate $H_1 < H < H_2$ state. We consider the energy function that governs ordering of the Ce 4*f* spins, which are represented by fixed-length (set to 1 here) vectors $\mathbf{S}_\alpha = (S^x{}_\alpha, S^y{}_\alpha, S^z{}_\alpha)$ that should be interpreted as the expectation value of the pseudospin describing the Kramers doublet ground state on the Ce sublattice α = A, B. Assuming ferromagnetic intrasublattice interactions, all spins within a single sublattice polarize identically, and the minimal model for the energy per unit cell is then

$$E = \mathrm{J}_\perp(S_A^x S_B^x + S_A^y S_B^y) + \mathrm{J}_z S_A^z S_B^z + \sum_\alpha [\mathrm{D}(S_\alpha^z)^2 - \mathbf{H}\cdot\mathbf{m}_\alpha] \quad (1)$$

where $\mathrm{J}_\perp, \mathrm{J}_z > 0$ are antiferromagnetic, and $\mathrm{D} > 0$ is an effective easy-plane anisotropy. The magnetic moments $\mathbf{m}_\alpha = \frac{\mu_B}{2}\mathbf{g}^\alpha\cdot\mathbf{S}_\alpha$, with the *g*-tensors $\mathbf{g}^A = \mathrm{diag}[g_{xx}, g_{yy}, g_{zz}]$ and $\mathbf{g}^B = \mathrm{diag}[g_{yy}, g_{xx}, g_{zz}]$. For the relation to microscopic exchange interactions, see (*29*). Within this model, for $2\mathrm{D} + \mathrm{J}_\perp > \mathrm{J}_z$, the zero-field ground state is such that the A and B spins are antialigned and lie in the (001) plane. Owing to the anisotropy of the *g*-tensor, the system has a nonzero net (ferrimagnetic) moment, consistent with the observed powder neutron diffraction (*29*). An infinitesimal field selects a direction for the spins via Zeeman coupling; the ordering pattern of **m** in small $\mathbf{H}\|[100]$ is shown in Fig. 3A. Crucially, the [100] magnetic field preserves the operation m'_{010} [i.e., the combination of the (010) plane mirror and time reversal], and the magnetic state is invariant under this transformation as well. Figure 3B summarizes the configuration of **m** on sublattice A and B with increasing *H*. For fields along <100>, the spins remain strictly antialigned, along **H**, up to a critical field (which we identify with H_1) where they acquire a nonzero in-plane component perpendicular to the field. With further increasing field, the magnetization increases until both spins are aligned along the field (at a field strength identified as H_2), where the aforementioned symmetry is recovered and a single domain exists. The intermediate "canted" phase (between H_1 and H_2) spontaneously breaks m'_{010}, and contains two types of magnetic domains: for $\mathbf{H}\|[100]$, the A spins can acquire $S^y{}_A > 0$ or $S^y{}_A < 0$.

We explain the resistivity anomaly and SAMR as follows. Without special preparation of the system, and for $\mathbf{H}\|[100]$, a sample in the canted phase generically contains a mosaic of domains.

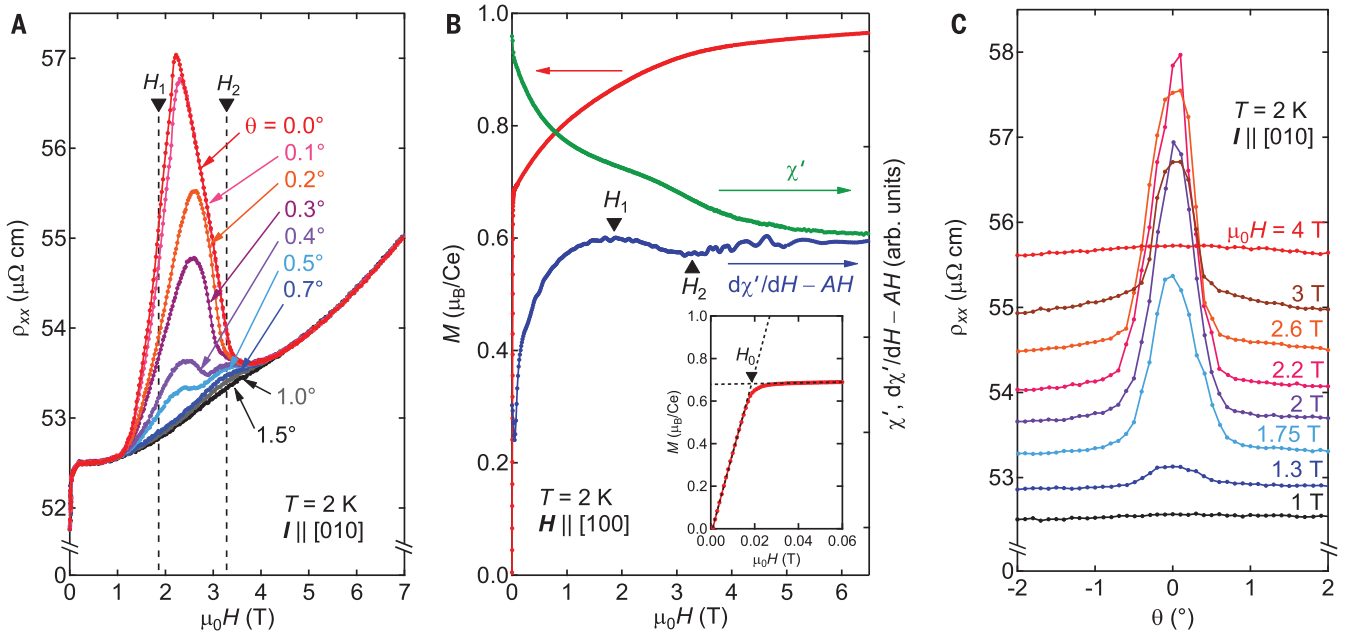

Fig. 2. Magnetic field dependence of SAMR. (**A**) Magnetic field H dependence of the longitudinal resistivity ρxx for different field orientations θ (defined in Fig. 1A). Electric current I direction is fixed along the [010] direction. The two critical field scales H_1 and H_2 are shown (see text). (**B**) Magnetization $M(H)$ and the real part of the ac susceptibility χ' and its field derivative with subtraction of the high H slope $d\chi'/dH - AH$, where the coefficient A is determined by fitting the data above $\mu_0 H = 4.5$ T. H_1 and H_2 are shown. The inset shows the low-H region for $M(H)$ where a sharp increase is observed up to H_0, which is defined as the crossing point of the linear extrapolation from the low- and high-H regions shown by dashed lines. H is applied along the [100] direction. (**C**) Angular θ dependence of ρ_{xx} around the [100] direction at several field strengths H. The directions of H and I are same with those in (A). The curves for $\mu_0 H$ = 1.3, 1.75, 2, 2.2, 2.6, 3, and 4 T are offset by 0.3, 0.6, 0.9, 1.2, 1.5, 1.8, and 2.1 microhm·cm, respectively.

Enhanced resistance naturally occurs at the domain boundaries. The m'_{010} symmetry is not explicitly broken (it is microscopically present) and hence can be broken spontaneously only for $\mathbf{H} \| [100]$. Even a small rotation of the field within the (001) plane breaks the m'_{010} symmetry explicitly and selects a single preferred domain. The consequent removal of DW resistance generates the observed SAMR signal. As shown in Fig. 2C, in a field $\mu_0 H = 2.2$ T this occurs at a tilt angle $\theta_t \approx 0.6°$, corresponding to a DW motion field scale $H\sin\theta_t \approx 230$ Oe, comparable to that observed in conventional magnets (*25*).

The above theoretical interpretation requires a high DW resistance for a large SAMR effect. We carried out ab initio density functional theory calculations using the full noncolinear magnetic structure and found a semimetallic band structure with Fermi surfaces consisting of small pockets proximate to Weyl nodes (*29*). The electronic structure is similar to that observed in LaAlGe (*35*), supporting the presence of Weyl points throughout the *R*AlGe family. We argue that a high DW resistance is germane to such strongly spin-orbit–coupled magnetic semimetals, because the strongly anisotropic interactions and overall antiferromagnetic nature of the ordering favor narrow DWs that strongly scatter the low-density electrons (*36*). Phase space alone places a lower bound on the DW resistance due to Fermi surface mismatch (Fig. 1C and figs. S13B and S22). Following a Landauer-Büttiker approach, electrons transmit across the wall and contribute to conduction only if they can preserve their transverse momentum at the Fermi energy; this requires overlap of the Fermi surfaces on either side. The overlap is minimized for small Fermi surfaces that are strongly displaced by magnetic order—exactly the conditions pertaining to magnetic nodal semimetals. We estimate the DW contribution to the macroscopic resistivity enhancement [see sections 13 and 14D of (*29*) for a general discussion and a band calculation, respectively] as

$$\frac{\Delta\rho}{\rho_0} \sim \frac{\ell}{L_w}\frac{1}{g} \qquad (2)$$

where ℓ is the bulk mean free path, L_w is the typical domain size, and $g < 1$ represents the fractional transmission of Fermi surfaces between the two domains (*29*). It is particularly desirable to apply real-space (*37*) and momentum-space (*36*) techniques along with dynamical analysis to probe the structure of the magnetic domains or, alternatively, to examine crystals with dimensions comparable to the domain size to directly probe L_w.

We next examine the phase space for SAMR. SAMR onsets below T_N, which itself is marked by a kink in $\rho_{xx}(T)$ and a peak of dM/dT (*29*). For $T < T_N$ features in $M(H)$ and $d\chi'/dH$ associated with H_0, H_1, and H_2 develop as summarized in the H-T phase diagram in Fig. 3C with the SAMR response $\delta\rho_{xx} = \rho_{xx}(T, H, \theta = 0°) - \rho_{xx}(T, H, \theta = 1.5°)$ shown as the color scale (*29*). Compared with the relatively subtle features in the thermodynamic measurements, the transport response sharply identifies the region $H_1 < H < H_2$ in which m'_{010} is spontaneously broken. We have also observed an enhancement in the transverse resistivity ρ_{yx}, which similarly highlights the SAMR phase (*29*).

We note several features of this symmetry-breaking SAMR region. First, we observe a tendency toward separation between the SAMR state and the zero-field critical point in Fig. 3C. Theoretical analyses using both symmetry-based Landau theory and a microscopic lattice model confirm that the canted phase must be disconnected from T_N (*29*). Furthermore, a substantial broadening is observed for SAMR for rotations out of the (001) plane (Fig. 4A). We calculate the corresponding phase diagram for **H** (Fig. 4B); the canted phase persists when the field is rotated within the (100) or (010) planes. Finally, we determine the zero-field ground state using the full model (*29*), including all weak anisotropies beyond those in Eq. 1, and find a specific noncolinear state with in-plane magnetizations, which collapses rapidly to the colinear one in a small field (which we associate with H_0).

Finally, we suggest key ingredients for realizing SAMR materials. Magnetically, the phenomenon relies upon strong anisotropy so that

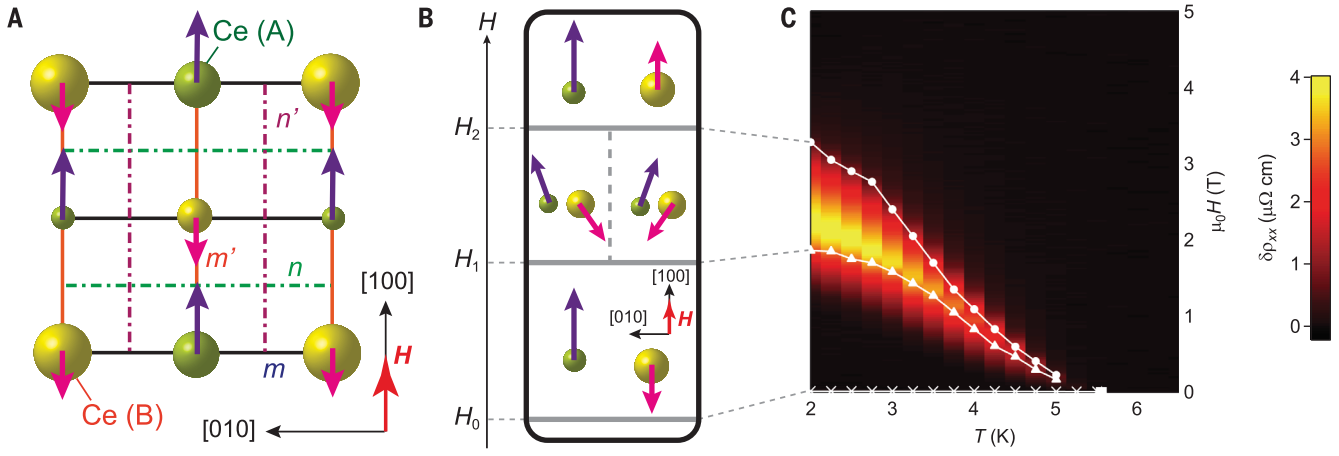

Fig. 3. Phase diagram of SAMR. (**A**) Model of the ordering pattern of the magnetic moment **m** with **H**∥[100] for $H_0 < H < H_1$, consistent with theoretical calculations and neutron scattering experiments. The underlying mirror plane (*m*), glide plane (*n*), and their time-reversal combined symmetry operations (*m*′ and *n*′) are also shown. (**B**) Theoretical evolution of the moment ordering with **H**∥[100]. The colinear order established above H_0 gives way at H_1 to a state with a spontaneous perpendicular component of the magnetization, breaking m'_{010}, with two degenerate configurations. At higher $H > H_2$, a colinear order is restored. (**C**) *H*-*T* phase diagram mapped by SAMR for **H**∥[100]. The cross, triangle, and circle symbols represent H_0, H_1, and H_2, respectively, derived from *M*, χ′, and *dχ′/dH*. The square symbol indicates the antiferromagnetic ordering temperature in zero field. The color scale is given by the SAMR signal $\delta\rho_{xx} = \rho_{xx}(T, H, \theta = 0°) - \rho_{xx}(T, H, \theta = 1.5°)$. The connection of this phase diagram to the predicted spin structure is shown with the dashed gray lines connected to (B).

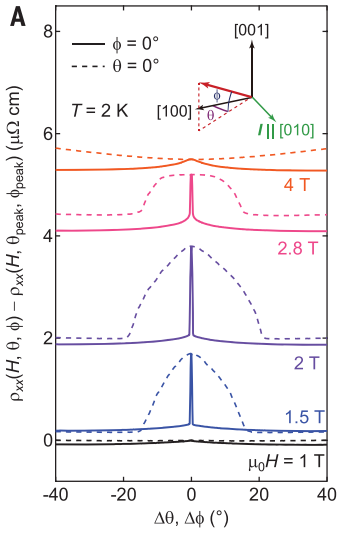

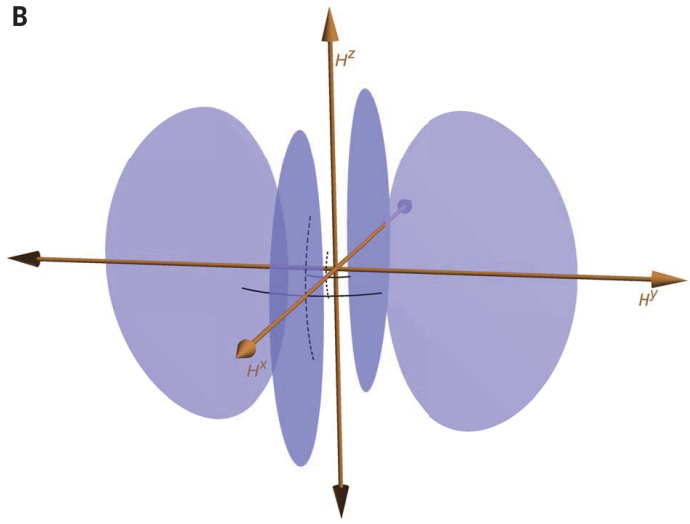

Fig. 4. Evolution of SAMR for field rotation out of the tetragonal plane. (**A**) Comparison of the observed SAMR signal for rotations in (θ, solid lines) and out of (ϕ, dashed lines) the *ab* plane. $\theta_{peak}(\phi_{peak})$ is the magnetic field *H* angle where the resistivity ρ_{xx} shows a maximum in the *H* rotation with fixed $\phi(\theta) = 0°$. $\Delta\theta(\Delta\phi)$ is the tilting of *H* measured from $\theta_{peak}(\phi_{peak})$. The curves for $\mu_0 H$ = 1.5, 2, 2.8, and 4 T are offset by 1.7, 3.8, 5.2, and 5.5 microhm·cm, respectively. (Inset) Definition of the angles that parametrize the orientation of the field. (**B**) Theoretically determined phase diagram of the SAMR phase (blue lobes) for arbitrary orientations of the field vector **H** and zero temperature. It is obtained by minimizing the mean field energy in Eq. 1; see section 11 of (*29*) (with $J_\perp = 4$, $J_z = 2$, $D = 1$, $g_{xx} = 1.2$, $g_{yy} = 0.8$, and $g_{zz} = 1$ in Eq. 1). The blue regions show the domains of spontaneous symmetry breaking (i.e., where there is spontaneous canting of the moments and a twofold ground-state degeneracy).

crystalline symmetries are fully communicated to the spins, as well as a relatively low exchange scale so that a state change can be affected by manageable fields. The response of the magnetism of CeAlGe to chemical substitution is useful in realizing such a ground state, which may serve as guide for further material realizations (*29*). Electronically, the Fermi surface mismatch leading to high-resistance DWs requires a semimetal with a small Fermi surface in close proximity to a node, and narrow bandwidth and strong coupling to the spins are beneficial. Note that specifically Weyl points are not essential, and Dirac or other nodal structures should suffice. The SAMR effect itself requires a magnetic point group operation (here m'_{010}), which remains a symmetry in a magnetic field along some specific axes, but not for other orientations, and that this symmetry is spontaneously broken in some parameter regime. Less abstractly, a deviation of the field from the prescribed axis must couple linearly to the order parameter of the canted phase. This condition requires that the canted phase must not break translational symmetry. Therefore, structures with multiple magnetic sites in the crystalline primitive unit cell are desired in the case of spin antiferromagnets. From Eq. 2, we see that the strength of the response $\Delta\rho/\rho$ is enhanced in cleaner systems with larger ℓ but smaller L_w. Optimized growth conditions may reduce the defect density to control the former (*29*), whereas device fabrication may allow for control of the energy and microstructure of magnetic domains responsible for determining the latter. As in transition metal–based magnets, the applied **H** is expected to affect the DW orientation and, in turn, modulate $\Delta\rho/\rho$ (*38*)—this is consistent with the observed breaking of <100> degeneracy for SAMR in Fig. 1B. More generally,

the angular sharpness of $\Delta\theta$ is limited by the pinning of the magnetic DWs. Reducing the pinning potential would allow SAMR to be narrowed toward the δ function response expected from theory. Engineering the SAMR behavior in materials with reduced electronic and magnetic defects for improved sensitivity or with magnetic 3d transition elements for higher T operation may provide pathways to devices capable of vector magnetic sensing with singular angular sensitivity (*39*).

REFERENCES AND NOTES

1. C. L. Kane, E. J. Mele, *Phys. Rev. Lett.* **95**, 146802 (2005).
2. J. E. Moore, L. Balents, *Phys. Rev. B* **75**, 121306(R) (2007).
3. L. Fu, C. L. Kane, E. J. Mele, *Phys. Rev. Lett.* **98**, 106803 (2007).
4. L. Liu *et al*., *Science* **336**, 555–558 (2012).
5. G. Jackeli, G. Khaliullin, *Phys. Rev. Lett.* **102**, 017205 (2009).
6. B. A. Bernevig, T. L. Hughes, S.-C. Zhang, *Science* **314**, 1757–1761 (2006).
7. M. Z. Hasan, C. L. Kane, *Rev. Mod. Phys.* **82**, 3045–3067 (2010).
8. X.-L. Qi, S.-C. Zhang, *Rev. Mod. Phys.* **83**, 1057–1110 (2011).
9. W. Witczak-Krempa, G. Chen, Y. B. Kim, L. Balents, *Annu. Rev. Condens. Matter Phys.* **5**, 57–82 (2014).
10. X. Wan, A. M. Turner, A. Vishwanath, S. Y. Savrasov, *Phys. Rev. B* **83**, 205101 (2011).
11. A. A. Burkov, L. Balents, *Phys. Rev. Lett.* **107**, 127205 (2011).
12. A. A. Soluyanov *et al*., *Nature* **527**, 495–498 (2015).
13. Z. Wang *et al*., *Phys. Rev. B* **85**, 195320 (2012).
14. S. M. Young, C. L. Kane, *Phys. Rev. Lett.* **115**, 126803 (2015).
15. S.-Y. Xu *et al*., *Science* **349**, 613–617 (2015).
16. Z. K. Liu *et al*., *Science* **343**, 864–867 (2014).
17. A. A. Zyuzin, A. A. Burkov, *Phys. Rev. B* **86**, 115133 (2012).
18. J. Xiong *et al*., *Science* **350**, 413–416 (2015).
19. H. Weng, C. Fang, Z. Fang, B. A. Bernevig, X. Dai, *Phys. Rev. X* **5**, 011029 (2015).
20. G. Xu, H. Weng, Z. Wang, X. Dai, Z. Fang, *Phys. Rev. Lett.* **107**, 186806 (2011).
21. G. Chang *et al*., *Phys. Rev. B* **97**, 041104(R) (2018).
22. J. Y. Liu *et al*., *Nat. Mater.* **16**, 905–910 (2017).
23. J. Kübler, C. Felser, *Europhys. Lett.* **108**, 67001 (2014).
24. K. Kuroda *et al*., *Nat. Mater.* **16**, 1090–1095 (2017).
25. I. Žutić, J. Fabian, S. Das Sarma, *Rev. Mod. Phys.* **76**, 323–410 (2004).
26. T. R. McGuire, R. I. Potter, *IEEE Trans. Magn.* **11**, 1018–1038 (1975).
27. S. K. Dhar, S. M. Pattalwar, R. Vijayaraghavan, *J. Magn. Magn. Mater.* **104–107**, 1303–1304 (1992).
28. A. M. Guloy, J. D. Corbett, *Inorg. Chem.* **30**, 4789–4794 (1991).
29. See supplementary materials.
30. S. Bobev *et al*., *J. Solid State Chem.* **178**, 2091–2103 (2005).
31. H. Flandorfer *et al*., *J. Solid State Chem.* **137**, 191–205 (1998).
32. H. Hodovanets *et al*., *Phys. Rev. B* **98**, 245132 (2018).
33. R. A. Borzi *et al*., *Science* **315**, 214–217 (2007).
34. C. Lester *et al*., *Nat. Mater.* **14**, 373–378 (2015).
35. S.-Y. Xu *et al*., *Sci. Adv.* **3**, e1603266 (2017).
36. B. G. Ueland, J. W. Lynn, M. Laver, Y. J. Choi, S.-W. Cheong, *Phys. Rev. Lett.* **104**, 147204 (2010).
37. T. Choi *et al*., *Nat. Mater.* **9**, 253–258 (2010).
38. M. Viret *et al*., *Phys. Rev. Lett.* **85**, 3962–3965 (2000).
39. J. Lenz, A. S. Edelstein, *IEEE Sens. J.* **6**, 631–649 (2006).
40. T. Suzuki, L. Savary, J.-P. Liu, J. W. Lynn, L. Balents, J. G. Checkelsky, Data for "Singular angular magnetoresistance in a magnetic nodal semimetal." Harvard Dataverse (2019); doi:10.7910/DVN/22SOYV

ACKNOWLEDGMENTS

We acknowledge discussions with T. Kurumaji and J. P. Paglione and technical support from D. Graf, Y. Zhao, and Z. Xu. **Funding:** This work was supported by in part by the Gordon and Betty Moore Foundation EPiQS Initiative, grant GBMF3848 (J.G.C.), and a postdoctoral fellowship grant GBMF4303 (L.S.). L.B. was supported by the NSF under grant DMR-1818533. J.-P.L. was supported by ARO grant W911-NF-14-1-0379. L.S. is also grateful for the hospitality and funding of the KITP, where part of this work was carried out under NSF grant PHY-1748958. We acknowledge the National Institute of Standards and Technology, U.S. Department of Commerce, in providing the BT-7 neutron facility used in this work. **Author contributions:** T.S. synthesized the materials and performed the electrical and thermodynamic measurements. L.S. and J.-P.L. performed theoretical calculations. T.S. and J.W.L. performed neutron scattering experiments. All authors contributed to writing the manuscript. L.B. and J.G.C. supervised the project. **Competing interests:** The authors declare no competing interests. **Data and materials availability:** The data in the manuscript are available from the Harvard Dataverse (*40*).

SUPPLEMENTARY MATERIALS

science.sciencemag.org/content/365/6451/377/suppl/DC1
Materials and Methods
Supplementary Text
Figs. S1 to S22
Tables S1 to S3
References (*41–63*)

22 January 2018; accepted 7 June 2019
Published online 20 June 2019
10.1126/science.aat0348

Singular angular magnetoresistance in a magnetic nodal semimetal

T. Suzuki, L. Savary, J.-P. Liu, J. W. Lynn, L. Balents and J. G. Checkelsky

Science **365** (6451), 377-381.
DOI: 10.1126/science.aat0348originally published online June 20, 2019

Mind the angle

Interplay between real- and momentum-space properties of materials can lead to exotic phenomena. Suzuki *et al.* studied electrical transport in the presence of a magnetic field in cerium-aluminum-germanium, a Weyl semimetal that also harbors magnetism (see the Perspective by Hassinger and Meng). As they varied the orientation of the applied field, they noticed spikes of resistivity sharply centered around the high symmetry axes of the material. The spikes were a c onsequence of the small overlap of Fermi surfaces—which "live" in momentum space—on either side of magnetic domain walls, which occur in real space. This extreme angular sensitivity may be useful in practical applications.

Science, this issue p. 377; see also p. 324